Energy & Environmental Science

Unbiased solar H2 production with current density up to 23 mA/cm2 by swiss-cheese black Si coupled with wastewater bioanode

Journal:	*Energy & Environmental Science*
Manuscript ID	EE-ART-12-2018-003673.R1
Article Type:	Paper
Date Submitted by the Author:	01-Feb-2019
Complete List of Authors:	Lu, Lu; Princeton University, Civil and Environmental Engineering Vakki , Waltteri ; San Diego State University, Department of Chemistry Aguiar, Jeffery; Idaho National Laboratory Xiao, Chuanxiao; National Renewable Energy Laboratory, Hurst, Katherine; National Renewable Energy Laboratory, Fairchild , Michael ; San Diego State University, Department of Chemistry Chen, Xi; Princeton university, Civil and Environmental Engineering Yang, Fan; San Diego State University, Department of Chemistry Gu, Jing; San Diego State University, Department of Chemistry; San Diego State University Ren, Zhiyong; Princeton University, Civil and Environmental Engineering

Unbiased solar H_2 production with current density up to 23 mA/cm^2 by swiss-cheese black Si coupled with wastewater bioanode

Lu Lu,[1,5,†] Waltteri Vakki,[2,†] Jeffery A. Aguiar,[3] Chuanxiao Xiao,[4] Katherine Hurst,[4] Michael Fairchild[2], Xi Chen,[1] Fan Yang[2], Jing Gu,[2*] Zhiyong Jason Ren[1,5*]

[1] Department of Civil and Environmental Engineering and Andlinger Center for Energy and the Environment, Princeton University, Princeton, NJ 08544

[2] Department of Chemistry and Biochemistry, San Diego State University, 5500 Campanile Drive, San Diego, California 92182, USA

[3] Idaho National Laboratory, Nuclear Materials Department, 2525 Fremont Avenue, Idaho Falls, Idaho 83415, USA

[4] National Renewable Energy Laboratory, Chemistry and Nanoscience Center, Golden, Colorado 80401, USA.

[5] Department of Civil, Environmental, and Architectural Engineering, University of Colorado Boulder, Boulder, Colorado 80309, USA.

† These authors contribute equally to this work

*Corresponding author e-mail: jgu@sdsu.edu, zjren@princeton.edu

Abstract:

Unbiased photoelectrochemical hydrogen production with high efficiency and durability is highly desired for solar energy storage. Here, we report a microbial photoelectrochemical (MPEC) system that demonstrated superior performance when equipped with bioanodes and black silicon photocathode with a unique "swiss-cheese" interface. The MPEC utilizes the chemical energy embedded in wastewater organics to boost solar H_2 production, which overcomes barriers on anode H_2O oxidation. Without any bias, the MPEC generates a record photocurrent (up to 23 mA cm^{-2}) and retains a prolonged stability for over 90 hours with high Faradaic efficiency (96−99%). The calculated turnover number for MoS_x catalyst during a 90-h period is 495471 with an average frequency of 1.53 s^{-1}. The system replaced pure water on the anode with actual wastewater and achieved waste organic removal up to 16 kg COD m^{-2} photocathode day^{-1}. Cost credits from concurrent wastewater treatment and low-cost design make photoelectrochemical H_2 production practical for the first time.

Introduction

Energy and water are two inextricably linked sectors which underpin economic and social development.[1-3] Water is needed for each stage of energy production, and energy is crucial for water distribution, treatment, and desalination.[3] For renewable energy sources such as solar, water has been used as an electron and proton source for artificial photosynthesis (APS).[4, 5] In this context, an integrated approach to address the challenges and opportunities of the energy-water nexus carries a good potential. Solar energy is inexhaustible and clean, and it carries enormous potential to become the main energy source for the future. However, because its diffuse and intermittent nature, processes such as APS are needed to convert solar energy to storable and transportable fuels and chemicals.[5]

Artificial photosynthesis for renewable H_2 production relies on a photoelectrochemical (PEC) process at a semiconductor and electrolyte junction. However, current APS systems face challenges in high cost, low efficiency and poor stability.[6, 7] The potential necessary for the water-splitting reaction (1.23V + ~0.5V overpotential) requires the use of wide-bandgap semiconductors to generate sufficient voltage.[8-11] However, their wide bandgap precludes efficient utilization of the solar spectrum, which limits their efficiency. Low bandgap and low-cost materials such as silicon are desired to absorb a high fraction of the incident solar spectrum. Unfortunately, the PEC process with silicon has only been realized by adding three or four semiconductor junctions or an external source of electricity.[12] With many single junction

PEC semiconductors, it is also difficult to achieve water splitting at an unbiased condition due to unmatched band edge positions. Dual junction PEC electrolyzers can achieve unassisted H_2 production at reasonable current densities (12-18 mA/cm^2 at 1 sun), but the high cost of III-V semiconductor materials and problems of photoelectrode corrosion have made commercialization very difficult.[7, 13] Furthermore, previous APS research focused mainly on energy conversion efficiency and relied on high-purity water, often neglecting the economic and energetic cost of producing it. Clean water is not widely available, and purifying water requires significant cost and energy input. Therefore, if wastewater can replace pure water, the applicability of APS can be greatly expanded. Wastewater is generated anywhere human beings are present, and it is readily available and free. By integrating APS with wastewater treatment, both energy and water problems can be solved.

Microbial photoelectrochemical (MPEC) system utilizes the chemical energy embedded in wastewater organics to give a microbial boost to accomplish non-biased solar H_2 production. In this process, microorganisms oxidize waste organics rather than water to provide electrons to quench photoinduced hole h^+ on the semiconductor photocathode. Since microbial electrochemical oxidation (MEO) has much lower potential (~ –0.29 V vs. NHE at pH = 7, T = 298.15 K, P = 1 atm) than that of water oxidation (0.82 V vs. NHE) under the same condition, it dramatically reduces the thermodynamic energy required for H_2 production from 1.23 V (water splitting) to 0.12 V and leads to a negative shift of oxidation potential by 1.1 V (0.82 to –0.29 V vs. NHE).[14] Thus, the band-edges of most semiconductors can straddle the potentials of MEO

and hydrogen evolution reaction (HER) to achieve an unassisted H_2 production. It is worth noting that MPEC process here is different from conventional use of sacrificial reagents to scavenge hole in a photocatalytic reaction.[15] Sacrificial reagents are artificial additions with high cost, while organics in the wastewater are contaminants that need to be treated anyway. Plus, compared with a few reagents available, MPEC can theoretically utilize any biodegradable compounds. Moreover, the conversion products from the sacrificial reaction can be environmental contaminations or H^+ sink. Though MPEC systems have been previously attempted under both bias and unassisted conditions, the current density was orders of magnitudes lower than the solar H_2 conversion benchmark of 10 mA cm^{-2}, and no study investigated real wastewater operation to demonstrate system stability and practicability.[14, 16-21] For example, *p*-type Cu_2O photocathode only generated 0.05 mA/cm^2 for 30 minutes due to photo-corrosion and slow electron transfer dynamics,[16] and TiO_2 generated up to 1.25 mA cm^{-2} and lasted for only 10 min.[18] Our previous work coupled $GaInP_2/TiO_2/MoS_x$ photoelectrode with a bioanode showed an 24 hours stable photocurrent density of 0.42 and 7.7 mA cm^{-2} with 0 and 0.8 V external bias, respectively, but the high cost of the $GaInP_2$ prevented it from commercialization.[14]

In this study, we made breakthroughs by developing an inexpensive nanostructured black silicon (b-Si) photocathode with a "swiss-cheese" interface, and we coupled it with electroactive microbial-bioanodes in real brewery wastewater. B-Si is being increasingly used in solar energy

conversion due to its excellent properties in light absorbing, charge transport, and low cost,[22-24] but it suffers from degradation problem due to easy surface oxidation. To address this problem, a protection layer (e.g. TiO_2) is usually applied to stabilize the photoelectrode and catalyst interface. However, we demonstrated here that by developing a novel unique "swiss-cheese" interface b-Si can be extremely durable and efficient even without an oxide protection layer. We also utilized a bipolar membrane and two bioanodes in MPEC system to facilitate HER (Fig. 1). Both advances in material and reaction kinetics lead to generation of a record high and stable photocurrent (up to 23 mA cm^{-2}) for over 90 hours before the substrate ran out. More importantly, the operation of this system didn't need any external bias. The photoinduced H_2 production rate was orders of magnitude higher than those of reported MPEC systems, and even higher than that state-of-the-art unassisted PEC water splitting systems.[13] High rate wastewater treatment was also accomplished, greatly expanding the use and lowering the cost of artificial photosynthesis. The photocathode is a nanostructured variant of the Si solar cells that have been industrially-scaled to 100 GW annual production levels, so they could quickly be produced for commercial-scale MPEC systems at a low cost.

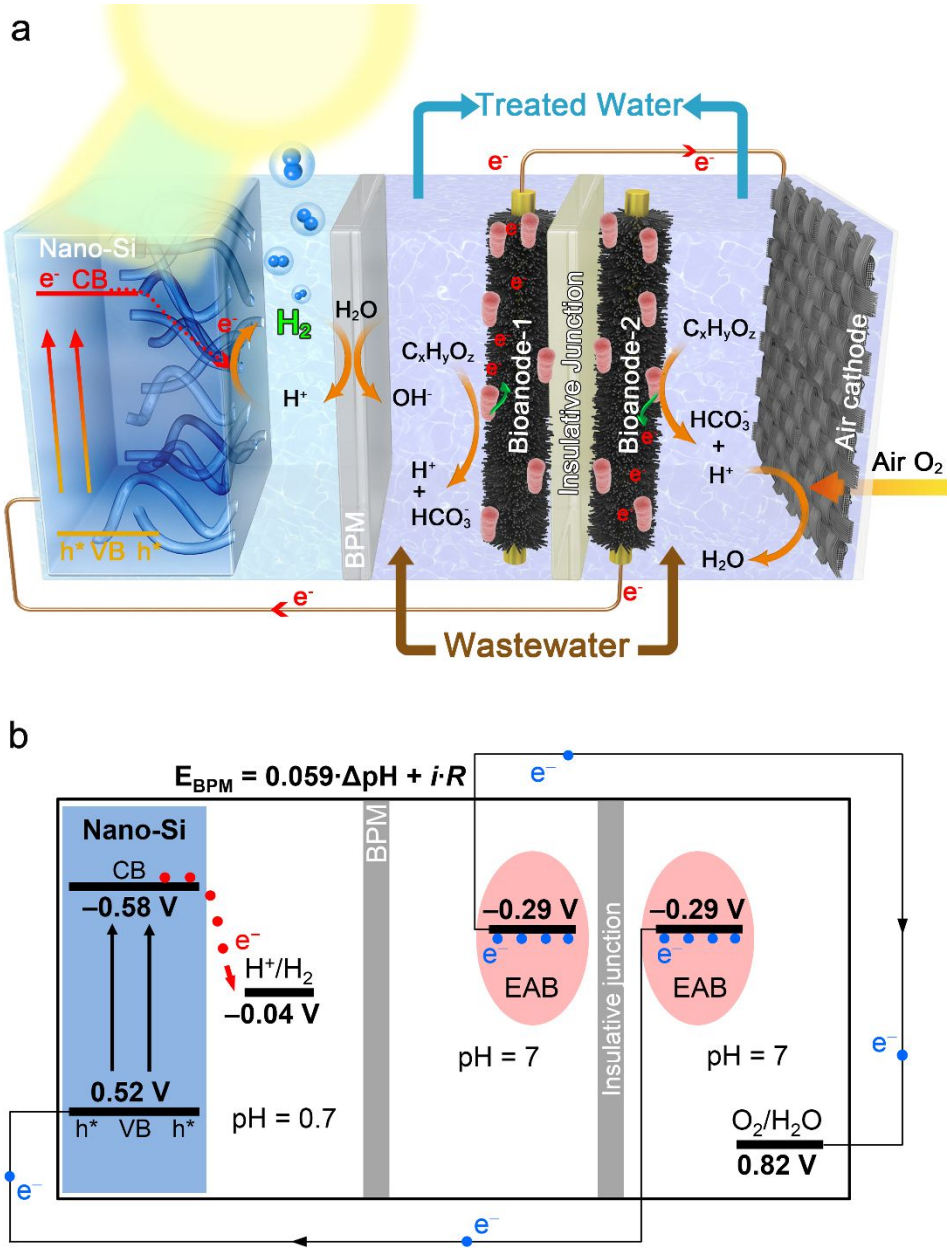

Fig. 1. Mechanism of the microbial photoelectrochemical (MPEC) system for high rate H_2 production using wastewater and sunlight. (**a**) Schematic of the MPEC configuration, where two anodes were coupled with a photocathode and an air-cathode. (**b**) Corresponding diagram of the carrier separation and charge transfer. CB and VB represent conduction band and valence band of semiconductor, respectively. Red and blue dots highlight the electrons generated by semiconductor and electroactive bacteria (EAB), respectively. Symbol "h*" represents the photo-induced holes in semiconductor. The thermodynamic potentials (vs. NHE) of H^+/H_2, O_2/H_2O and organics oxidation by EAB, band edges of CB and VB under zero bias, and the voltage drop over the bipolar membrane (E_{BPM}) are indicated.[7, 14, 25, 26]

Results

Synthesis and Characterization of the b-Si/Pt and b-Si/MoS_x Photoelectrodes

The b-Si was synthesized by metal-assisted chemical etching due to its simplicity, low-cost and versatility.[27] To enable high efficiency hydrogen evolution reaction (HER), MoS_x or Pt catalysts were further deposited on the top of the photoelectrodes (forming b-Si/MoSx and b-Si/Pt), where Pt was used as a benchmark control. The nanoscale interface structure and its chemical properties were investigated by a suite of tools including scanning electron microscopy (SEM), scanning transmission electron microscopy (STEM), electron energy loss spectroscopy (EELS), and others. The microscopic results demonstrate the "swiss cheese" interface is very different from a regular b-Si, filled with nano-porous vertical channels. While similar densely and randomly collocated pores ranging from 20-100 nm are shown on planar view (Fig. S1), the cross-section images show the structure contains tortuous channels angled in different directions to a depth of ~300 nm from the surface (Fig 2a, b). STEM and EELS spectra further resolved the detailed interface architecture with less than 1 nm resolution. Fig. 2a, b, c show the high annular dark (ADF) and bright (ABF) field STEM images, which demonstrate that MoS_x catalysts were deposited on the electrode and formed individual or continuous islands (300-500 nm) and its composition was further evidenced by the EDS (Fig. 2i, j), together with other elements (Fig. 2g, h). Higher resolution STEM images in 5 nm scale (Fig. S2b, d) demonstrate both MoS_x and SiO_x are amorphous in nature. Fig. 2c and Fig S2a, c reveals the clear morphology of tracks in the sample, where a significant portion of tracks terminate in parallel to the viewing direction. Each

150 track shows a depth of 100-300 nm and a width of 50-100 nm. The thickness of SiO_x walls at the
151 edge of track was measured to be less than 5 nm, which was further confirmed by higher
152 resolution cross-section STEM images (Fig. 2d, e, f and Fig. S2b, d). In the XPS analysis, three
153 Mo 3*d* doublets, which are attributed to the formation of Mo (IV) (as MoS_2), Mo(V) (as
154 MoO_xS_y), and Mo(VI) (as MoO_3) were recognized, and the separate binding energies were 229
155 eV, 230.3 eV and 232.8 eV, respectively (Fig. 2k). The S 2*s* peak at 226.5 eV indicates the
156 formation of S^{2-} and is consistent with the formation of Mo (IV). The S 2*p* spectra were reviewed
157 into three doublets as well, assigning into S_2^{2-} (162.5 eV), S^{2-} (161.8 eV) as well as electron-rich
158 sulfur phase (161.6 eV) (Fig. 2l).[28] Additional S 2*p* peaks at higher binding energy of 168.3 eV
159 were attributed to the formation of sulfate, resulting from the possible formation of
160 sulfur-oxygen bond.[29] The sulfur-oxygen bond might generate from interaction in between SiO_2
161 and MoS_x.
162

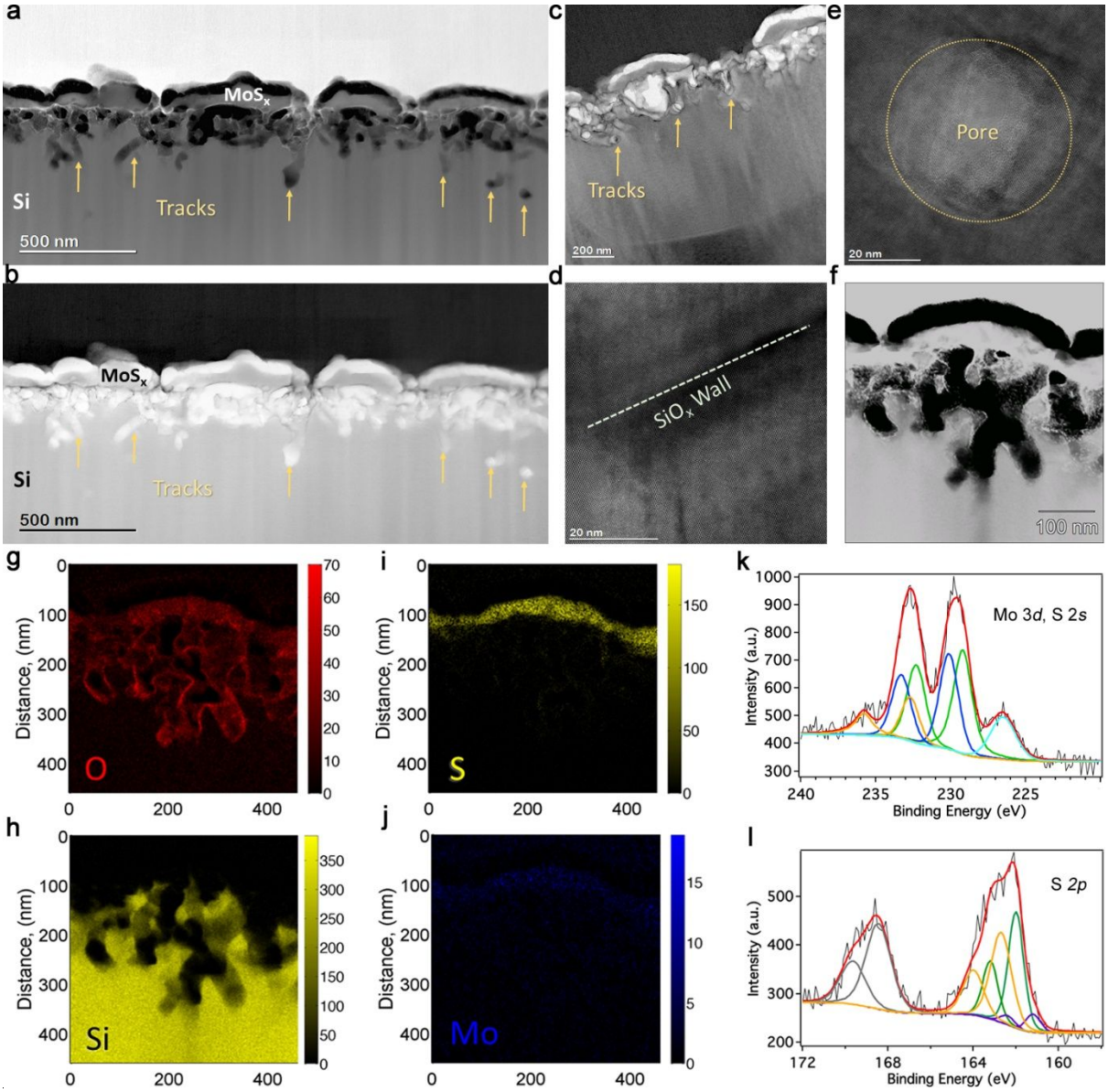

Fig. 2. Characterizations of b-Si/ MoS_x interface. (**a**) bright and (**b**) dark field STEM images present the interface morphology, (**c**) tracks concentrated near the surface, (**d**) SiO_x layer is further explored at high-resolution, revealing amorphous phase structure (**e**) tracks pore site with a thin SiO_x layer (15 nm), (**f**) STEM dark field image with EDS: (**g**) oxygen, (**h**) silicon, (**i**) sulfur, (**J**) molybdenum, (**k**) XPS spectra of Mo 3*d*, S 2s and (**l**) S 2p reveals that the presence of an intact MoS_x layer.

Different from MoS_x, Pt nanoparticles were located at the different depths in the tracks (Fig. S3a, b). Most of them located on the electrode's surface (Fig. 3a, b, c), while some nanoparticles

penetrated the interior of the irregular channels (Fig. 3d, e, f and Fig. S3a, b). Fig. 3d, e, f captured an image centered on a single-track, which reveals additional details on the track morphology with a platinum nanoparticle located at the very end of a twisted channel. The STEM-EDS further confirms the presence of different elements at the Swiss cheese interface (Fig. 3h-j). From the XPS spectra, the platinum 4*f* electron spectra are well resolved with two sets of doublet at binding energies of 71.2 eV and 72.6 eV (Fig. 3k). The lower binding energy peak indicates the formation of the metallic Pt (0), while the higher binding energy might result from the formation of a Si-Pt species or PtO by platinum nanoparticle interfacing with SiO_2.[30] The Pt and MoS_x catalysts loading amounts were 67.80 nmol/cm^2 and 97.16 nmol/cm^2, respectively.

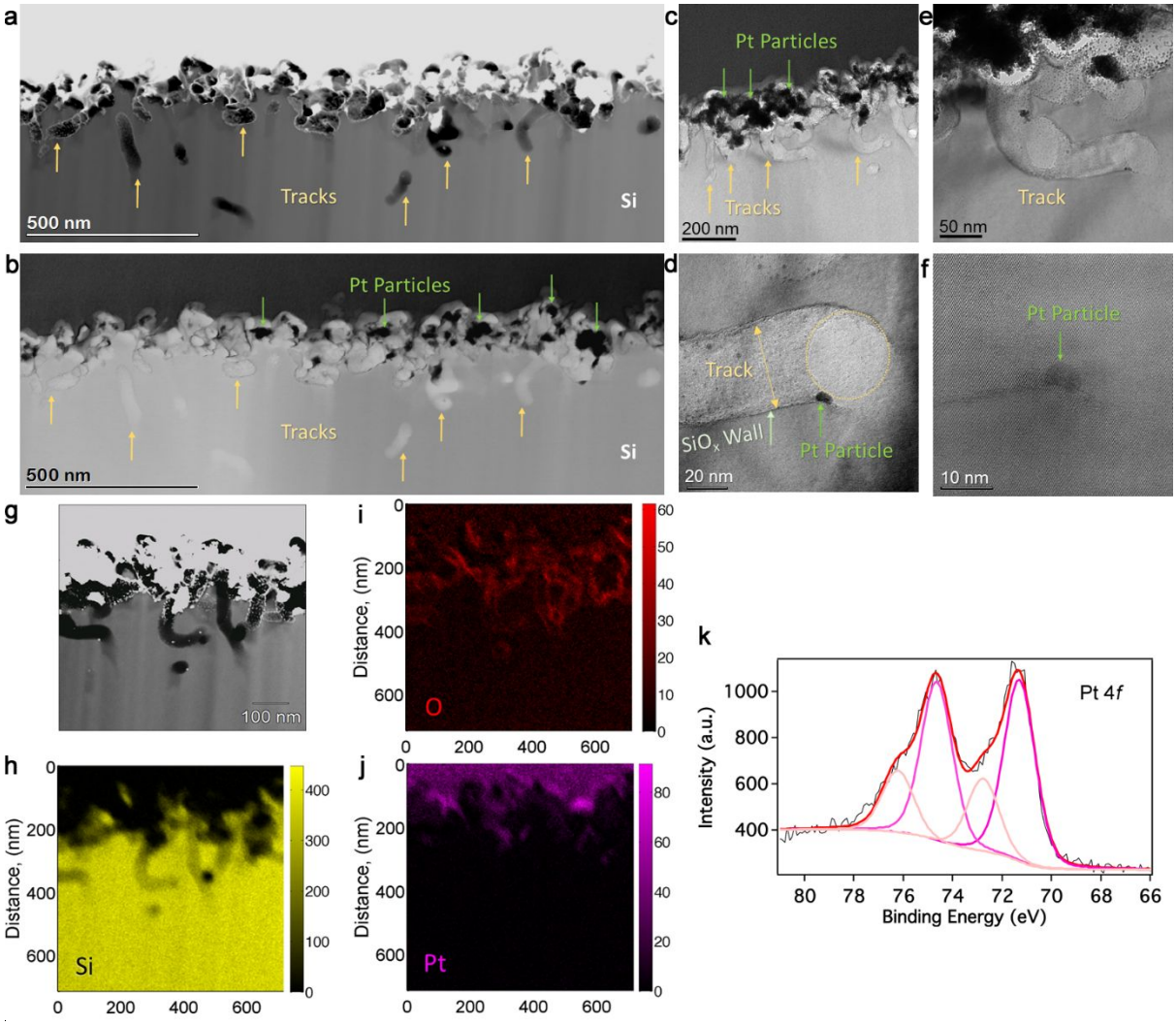

183

184 **Fig. 3. Characterizations of b-Si/Pt interface.** (**a**) bright and (**b**) dark field cross-section
185 images, (**c**) platinum nanoparticle aggregates at the surface, (**e**) single track that extended into
186 300-400 nm depth from the surface and, (**d**)(**f**) one platinum particle found that buried down in
187 the track. Over the same field of view, combining (**g**) STEM dark field imaging and
188 point-resolved EDS imagines: (**h**) silicon, (**i**) oxygen, (**j**) platinum. (**k**) The XPS spectra of
189 platinum catalyst modified electrode. The STEM-EDS shows the chemical distribution of
190 elements over a 700 nm × 700 nm square area containing several tracks shown in Fig. 3g, where
191 Si, O, and Pt are plotted as a function of residual net counts (Fig. 3h-l).

192

193 **Photo/electrochemical performance of the photocathodes and bioanode**

194 The catalytic property of the photocathodes was characterized using linear sweep voltammetry

195 (LSV) in 0.2 M H_2SO_4 (pH ~ 0.7) under 1 sun illumination (Fig. 4a). The two types of

photocathodes exhibited a similar photocurrent onset potential (V_{op}) of 0.38 V vs. reversible hydrogen electrode (RHE). However, b-Si/Pt showed a higher short-circuit photocurrent density (J_{sc}) (19.5 mA cm^{-2}) than that of the b-Si/MoS_x (9.2 mA cm^{-2}) at a bias of 0 V (vs. RHE). The solar to hydrogen (STH) conversion efficiency of the photocathode (η) used to examine the intrinsic efficiency of the photoelectrode alone[6] was 0.6% (b-Si/MoS_x) and 1.6% (b-Si/Pt). These results are comparable with the state-of-the-art b-Si photoelectrodes with V_{op} of 0.12–0.87 V, J_{sc} of 5.5–35 mA cm^{-2} and η of ~3.1%.[31] Without catalysts, the control b-Si electrode showed much lower V_{op} (0.11 V) and J_{sc} (0.5 mA cm^{-2}). Both b-Si/MoS_x and b-Si/Pt electrodes showed consistent limiting photocurrent densities of 28–30 mA cm^{-2}. The dark currents are negligible (~10^{-6} mA cm^{-2}) compared to the photocurrents. A control experiment was performed in a pH neutral condition, and a much lower J_{sc} 1.5–2.0 mA cm^{-2} was observed despite a constant V_{op} (Fig. S4). The incident photon-to-current efficiencies (IPCE) of Swiss-cheese electrodes (Fig. S5) were measured in 0.2 M H_2SO_4 solution at −0.6 V vs Ag/AgCl, where the contribution from dark current is minimal (Fig. 4A). The IPCE maximized at 65% at 650 nm. This is close to the value of previously reported nanostructured n+p-Si photoelectrode,[32] showing a desirable light-to-current conversion efficiency for swiss-cheese b-Si.

The electrochemical activities of the mature bioanode grown in brewery wastewater were characterized using turnover cyclic voltammetry (CV). The cyclic voltammogram demonstrated a typical sigmoidal shape with a single inflection point at the potential of ~ –0.347 V (vs.

Ag/AgCl) (Fig. 4b and inset, Fig. S6), at which the catalytic current reached the maximum value. This potential matched the reported midpoint potential of *Geobacter sulfurreducens*, which is known as a model electroactive bacteria (EAB),[33] and microbial community analysis confirmed that *Geobacter* sp. were dominant on the bioanodes (Fig. S7). These findings suggest that *Geobacter* sp. served as the primary EAB species responsible to extracellular electron transfer. SEM images of bioanodes clearly show bacteria tightly colonized on the surface of solid carbon fiber electrodes, and rod shaped cells dominated the anode (Fig. S8). Non-turnover CVs were performed under either readily degraded organics (electron donors) in wastewater were depleted, or under fresh electrolyte where no possible cell-excreted electron mediators were present. The same redox peaks were observed in both conditions, suggesting that the anode extracellular electron transfer was carried out by biofilm-bound redox compounds such as outer-membrane bound cytochromes rather than soluble electron mediators. It is also interesting to see that the microbial community structure shifted dramatically. Fig. S7 and S9 shows that *Lactobacillus* and *Simplicispira* were dominant in the initial brewery wastewater and anaerobic sludge inoculum, respectively, but *Geobacter* species were greatly enriched on the anode after operation, demonstrating that a robust and effective microbial community was established for both real wastewater treatment and current generation.

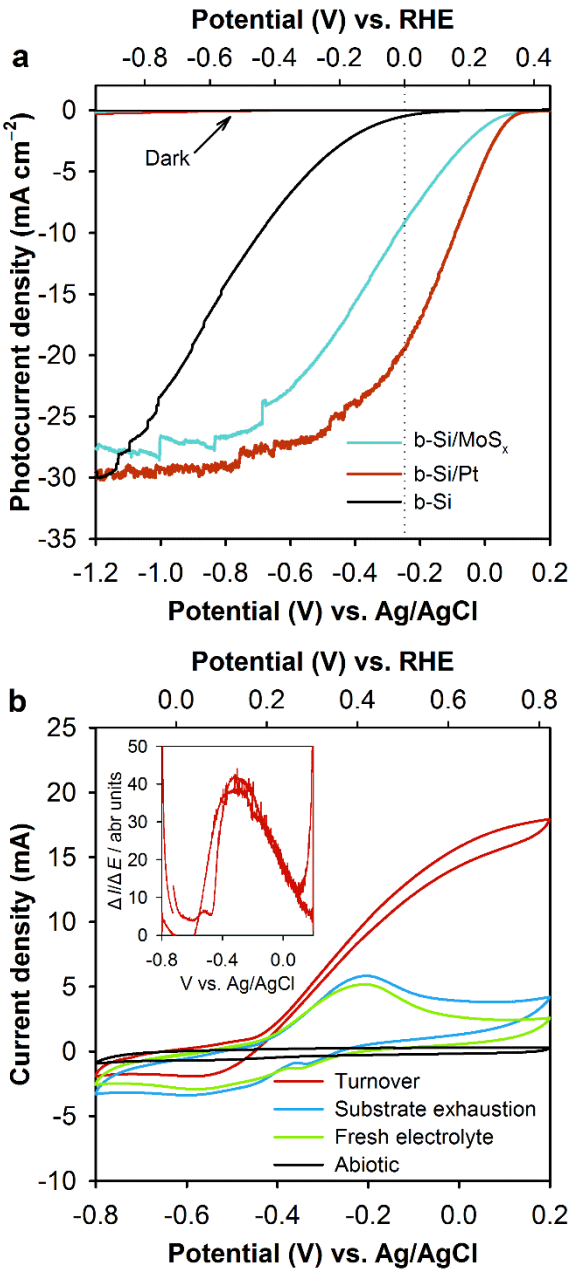

Fig. 4. Electrochemical characterizations of the photocathodes and bioanode. (a) Photocurrent density-potential (*J-V*) curves of b-Si/Pt and b-Si/MoS_x photocathodes. Scans were performed at 10 mVs^{-1} in 0.2 M H_2SO_4 (pH∼0.7) under 1 sun illumination or dark condition. (**b**) Cyclic voltammogram of the bioanode under turnover condition (red line) when operated in brewery wastewater (BWW) with the maximum biofilm activity, and under non-turnover condition with exhaustion of substrate in electrolyte (blue line) or in a fresh electrolyte without substrate (green line). The scan rate was 5 mVs^{-1}. An abiotic anode was also scanned as control (black line). Inset: first derivatives of the turnover CV.

Photocurrent generation in the MPEC system

Fig. 5a and 5b demonstrated the *I-t* curves in the chopped light experiment. MPEC reactors were equipped with two bioanodes and one photocathode, either b-Si/MoS_x or b-Si/Pt, respectively. Both systems obtained high photocurrent densities, and b-Si/Pt demonstrated higher output (21−23 mA cm^{-2}) than that of b-Si/MoS_x (16-19 mA cm^{-2}). Since the photocurrent density is directly correlated with the light response of the photocathode, negligible current was observed under dark condition. Both systems remained very stable in current output without much decay. Instead the current with the b-Si/MoS_x photocathode steadily increased with the time of operation. This might be attributed to structure reorganization of MoS_x catalysts during the electrolysis.[34]

Fig. 5c and 5d depict the potentials of the bioanode and photocathodes during the chopped light test. The bioanode potentials remained very stable, indicating steady microbial electrochemical reactions during wastewater treatment. A single bioanode coupled with a photocathode is able to sustain H_2 production without any external bias (Fig. S10a), because a bioanode can supply a maximum electrical bias of around -0.29 V (vs. NHE) (or -0.5 V vs. Ag/AgCl) to the photocathodes (Fig. S10c), which can theoretically generate a short-circuit photocurrent density at 20−26 mA cm^{-2}, reaching the limit photocurrent densities of Si electrode based on the photocathode's electrochemical performance (Fig. 4a). However, in the actual experiment the bipolar membrane (BPM) increased the internal resistance and led to a voltage drop of

263 approximately 0.38 V (Fig. S10d, Fig. 5e, f). This reduced potential gradient resulted in a lower
264 self-sustaining current density of 1.8 mA cm^{-2} (Fig. S10b). The voltage drop caused by BPM can
265 be attributed to the Ohmic loss ($i \cdot R$) and driving force required for water dissociation
266 ($0.059 \cdot \Delta pH$).[26] Where, i (A cm^{-2}) and R ($\Omega \cdot cm^2$) are current density and area resistance of the
267 BPM, respectively, and ΔpH is the pH difference over the BPM. However, BPM was employed
268 since its excellent capability to maintain the pH gradient and minimize salt cross-over as
269 compared with other separators[26] (Fig. S11). To maintain the high current, a third chamber was
270 added with a second anode (Bioanode-2) and an air cathode (Fig. 1). This modification provided
271 an additional bias of 0.5−0.6 V (green line in Fig. 5e, f and S12e, f), which shifted the
272 photocathode potential to -0.5 − -0.65 V vs. Ag/AgCl (purple line in Fig. 5c, d and S12 c, d) and
273 easily jump-started the current density to a much higher level at ~23 mA cm^{-2}. For our system,
274 due to the advancements made in materials and configurations, the small self-sustaining bias was
275 sufficient to boost the photocurrent to the saturated value. However, it is not the case in other
276 MPEC or PEC systems. For example, a 0.8 V bias only boosted photocurrent density from 0.42
277 to 7.7 mA cm^{-2} on a previous MPEC over 24 hours,[14] and a PEC boosted by a bioanode and an
278 oxygen reduction cathode only generated a photocurrent density of 1.23 mA cm^{-2} for 10 min.[18]
279
280 To improve the scalability of the system and enable both sustainable wastewater treatment and
281 efficient hydrogen generation, optimizations can be made to reduce internal losses and improve
282 the reaction rates. This may include increasing the surface area of the electrodes and the

283 membrane, reduce electrode distance, and change electrolyte.[35] In the current lab scale system,
284 the bioanode surface area (0.22 m^2) is orders of magnitude higher than that of the photocathode
285 (~0.1 cm^2). This is necessary because the rate of biological reactions can be much slower than
286 photocatalytic reactions, and the need of wastewater treatment requires large liquid volume. It is
287 estimated that 1 m^2 of photocathode would be matched with 1.2 m^3 of carbon brush anode with
288 specific surface area of 18000 m^2 m^{-3}. This difference is rather an advantage, as it allows more
289 efficient wastewater treatment by providing a larger anode surface, while it saves on the cost of
290 the photocathode. The use of acidic catholyte (0.2 M H_2SO_4, pH ~0.7) for H^+ reduction
291 dramatically improved the performance of MPEC, which could increase the current density by
292 orders of magnitude compared with neutral catholyte.[14]

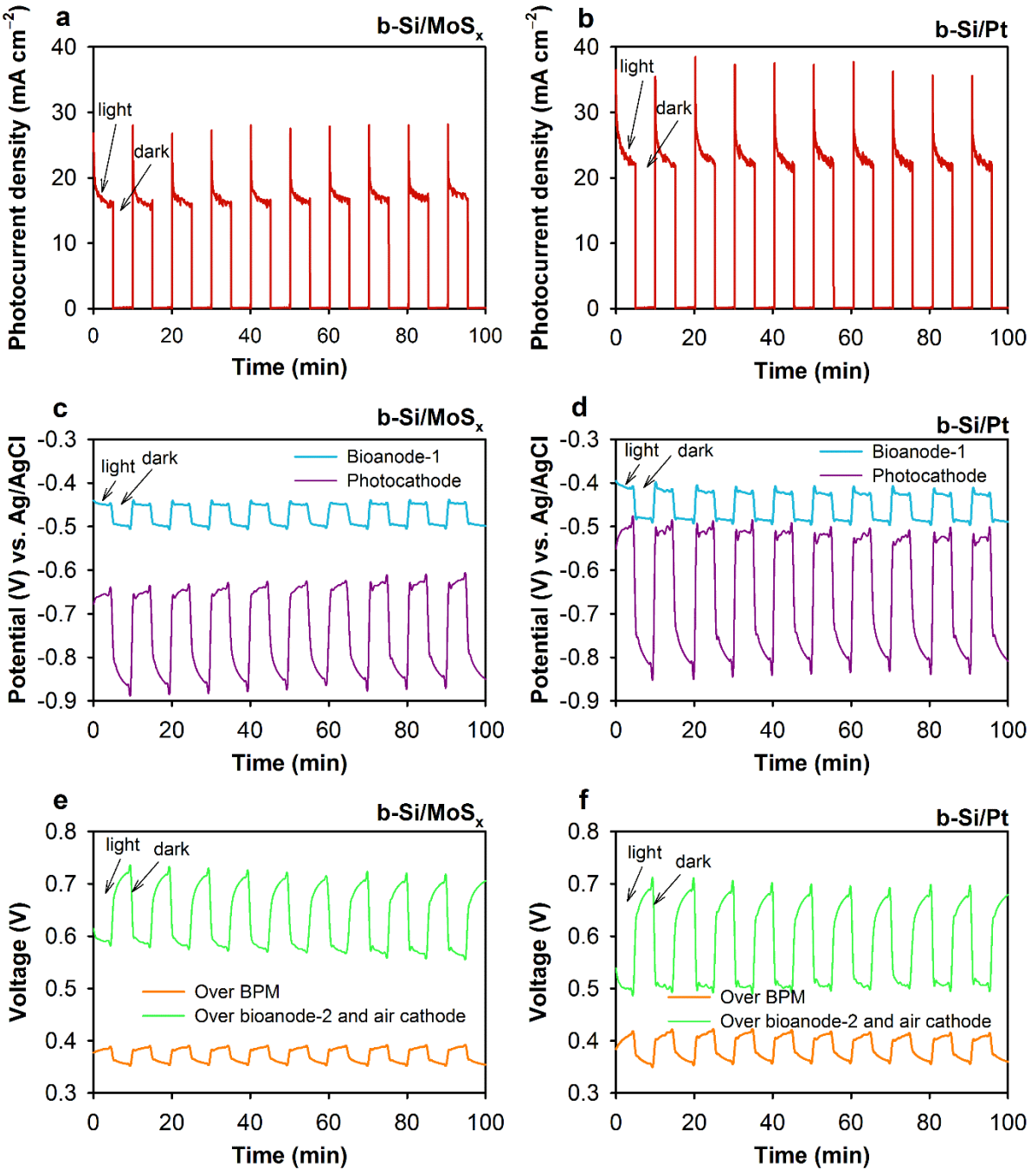

Fig. 5. Characterization of MPEC with different photocathodes under 1 sun on/off illumination. (**a**) and (**b**). Photocurrent density-time (*J-t*) curves. (**c**) and (**d**). Electrode potentials of MPEC. **e**, **f**, Voltage drop over bipolar membrane (BPM), and voltage over bioanode-2 and air cathode that serves as a bias for photocathode. The MPEC was fed with actual brewery wastewater (BWW).

300

301 **MPEC system durability for sustainable H_2 production with wastewater treatment**

302 Few self-sustaining APS reactors achieved good performance, and the main bottlenecks are
303 related to the efficiency, stability, and costs of the photocatalysts. Compared with previous
304 MPEC attempts, this study is significant. For the first time, it demonstrates a stable high current
305 at ~23 mA m^{-2}, which lasted for more than 90 hours using both low-cost nanoporous Si based
306 photocathodes. Fig. 6 shows the long duration and stability of the photocurrent till the end of the
307 experiment. Duplicate MPEC reactors equipped with b-Si/MoS_x photocathodes showed very
308 similar performance. The photocurrent showed a quick increase in the first 4 hours before
309 reaching to the maximum level of 20–23 mA m^{-2}. The system kept stable in the next ~70 hours
310 before a gradual decline to 17-18 mA m^{-2} till 90 h with only ~28% initial current lost. In
311 comparison, the b-Si/Pt systems showed less fluctuation, and the photocurrent stabilized at 23-24
312 mA m^{-2} for ~50 hours before small decline to 18–20 mA m^{-2} at the end of 90-h test with only
313 ~25% initial current lost (Fig. 6). High Faradaic efficiencies (96–99%) and a linear relationship
314 between the photocurrent and H_2 production were observed in all systems, indicating very
315 efficient conversion of photoelectrons to H_2 (Fig. 6 insets). The calculated turnover number
316 (TON) and turnover frequency (TOF) for 90 h were 388768 and 1.20 s^{-1} for b-Si/Pt and 495471
317 and 1.53 s^{-1} for b-Si/MoS_x electrode, respectively.

318

319 The electrode potentials, voltages drop over BPM, and voltages over bioanode and air

cathode were recorded during the durability testing (Fig. S13). These data were well-aligned with the chopped light experiment (Fig. 5) and demonstrated extremely high stability. For organic removal from wastewater measured by chemical oxygen demand (COD), the bioanode served the major role and removed 4 and 10−12 kg COD m^{-2} photocathode day^{-1} by the bioanode 1 and 2, respectively (Fig. S14). Coulombic efficiencies that represent the conversion efficiency from substrate to current were 35−37% and 13−14% for the bioanode 1 and 2, respectively (Fig. S15). The real-time H_2 production is recorded as a video clip provided in Supplementary Information (Fig. S18). The lower Coulombic efficiency observed for bioanode 2 can be explained by the air diffusion from the air cathode, which facilitates non-electroactive microbial growth (see details in Supplementary Information).

Compared with most other black silicon interfaces that lasted for a few hours,[22, 36] this swiss-cheese interface was found to be very stable even in a strong corrosive environment. The stability of this unique interface (b-Si/pt) was further compared with a normal straight channel b-Si (Fig. S19) with platinum under various pH by LSV. As demonstrated in Fig. S20, column B-Si was extremely unstable under all pH conditions (pH=1, 7, 12.5), with a change of ~ 200 mV, ~ 100 mV and ~ 400 mV, respectively, between the first and the fourth run. While the swiss-cheese interface was stable under acidic or neutral condition but showed a slight degradation of 50 mV under basic condition. Moreover, under all these conditions, the swiss-cheese electrode demonstrated a superior onset potential as compared with the normal

column Si based on the first LSV, with 0 mV, 200 mV, 400 mV difference at acid, neutral and basic conditions, respectively. The detailed mechanisms that led to the high stability is still under investigation.

For the post-electrolysis photocathode stability characterization, the top view and cross-section SEM images were demonstrated for both b-Si/MoS_x (Fig.S21 a, b) and b-Si/Pt (Fig.S21 c, d) electrodes. The b-Si/MoS_x mostly preserved its initial nanostructure while the b-Si/Pt demonstrated deterioration of its surface channel after electrolysis. Pt nanoparticles showed aggregated effect to form large nanoparticle (100−400 nm) while MoS_x layer formed islands. Further studies with an extended period of electrolysis will be performed to investigate the stability of these electrodes when decay of "swiss-cheese" structure occurred. The stability results further confirm that non-precious metal catalysts can achieve comparable and stable performance to traditional precious metal catalysts.

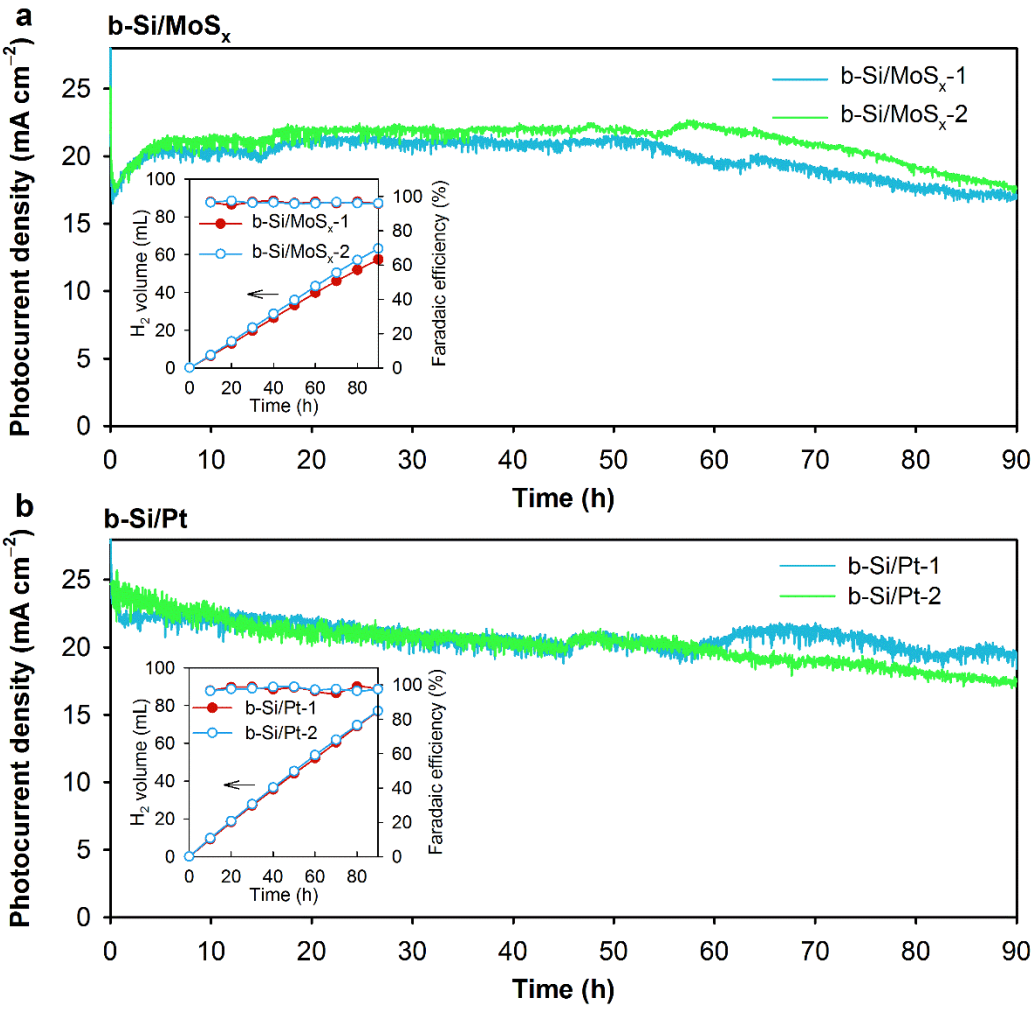

Fig. 6. Stability test of the MPEC. (a) and (b), 90 h photocurrent density-time (*J-t*) curves of MPEC with b-Si/MoS_x and b-Si/Pt photocathode, respectively. Duplicate testing was conducted by using two similar photocathodes named "1" and "2". The MPEC was fed with actual brewery wastewater (BWW). Inset: H_2 production and Faradaic efficiency (photocathode) of MPEC as a function of time.

Discussion

This MPEC system presents a breakthrough of photoelectrochemical H_2 production compared to previous studies. For the first time it used real wastewater as compared to artificial chemicals and generated record levels of photocurrent density for H_2 generation. Moreover, compared to a few

364 minutes or hours duration in previous MPEC, this system was operated for 90 h without
365 significant performance drop. Such superior performance demonstrates that this MPEC holds
366 great potential for real applications. Bipolar membrane was used here for water dissociation to
367 generate H^+ and OH^- for H_2 production and pH neutralization, respectively. This not only
368 maintained low pH or abundant H^+ source at the photocathode to facilitate H_2 evolution and but
369 also eliminated the need of H^+ diffusion from the anode, which has been a limiting factor in other
370 MPEC systems.
371
372 The performance of this MPEC system is comparable or even higher than most state-of-the-art
373 conventional photoelectrochemical (PEC) systems (Table S2). For example, a 12.4% (~10
374 mA/cm^2 photocurrent density) solar-to-hydrogen efficiency (STH) from a PEC with
375 multi-junction III-V semiconductor was a record for a long time.[8] Till recently another study
376 reported a 16% STH (~13mA/cm^2) by using an inverted metamorphic multi-junction
377 semiconductor.[37] However, the stability of above PEC systems is usually less than a few hours.
378 One of the best PV-electrolysis systems possessed a ~30% STH (~25 mA/cm^2 photocurrent
379 density) for 50 h, which was made by an expensive InGaP/GaAs/GaInNAsSb multi-junction
380 solar cell.[38] Our work demonstrated the such high current and longer duration can be achieved
381 without using noble catalysts rather low-cost semiconductors and real wastewater streams.
382
383 Preliminary cost estimates show that the H_2 produced from wastewater MPEC can cost < \$4 per

kg H_2 with combined capital and operating expenditures. This is based on comparison with hypothetical large-scale PEC water-splitting plants with tandem panel array and 8.1–12.2 mA cm^{-2} photocurrent density (10–15% STH efficiency).[39] This cost is lower than the US Department of Energy $4-7 per kg H_2 target by 2020.[40] MPEC will provide integrated and distributed wastewater and energy solutions to industries, households and communities. An ideal niche entry market can be the food and beverage industries which needs both high strength wastewater treatment and renewable H_2 source. In the U.S. approximately 0.76 billion m^3 of biodegradable food & beverage wastewater are generated per year,[41] which could generate 0.46 million tons of H_2 using MPEC processes by using a mean organics concentration of 5400 mg/L chemical oxygen demand (COD) and 90% conversion efficiency. This accounts for 5% of annual H_2 production in the U.S.[42] Another entry market can be decentralized or developing communities, where wastewater and sunlight are available, but they don't have water or energy infrastructure. MPEC will bring double benefits to these communities as it addresses both water and energy in one system.

Conclusion

An MPEC system prototyped here demonstrated superior performance in converting solar energy to renewable H_2 with concurrent wastewater treatment. The MPEC demonstrated a high average photocurrent of 20.5 mA cm^{-2} for over 90 h with up to 90-96% photocathode faradaic efficiency. By replacing anodic H_2O oxidation with organic oxidation in wastewater, the photovoltage

demand of the semiconductor is greatly reduced from 1.23 V to 0.12 V, so hydrogen evolution can occur spontaneously under solar irradiation with the use of the low-cost silicon. The inexpensive nanostructured black silicon (b-Si) photocathode with the "swiss-cheese" interface showed very high efficiency and great stability. The microbial anode treats wastewater and converts wasted chemical energy into electrical potential to eliminate the need for an external power source. This overcomes a major barrier faced by APS and opens tremendous opportunity for low cost H_2 production. Moreover, no O_2 is generated in the MPEC anode, and the use of wastewater to replace fresh water greatly expands the application, as wastewater is generated wherever there is human activity.

Methods

Photoelectrode fabrication with nano-porous black silicon and catalysts

Different from traditional steady state wet-etching, we introduced organic solvents, which led to the formation of high tortuosity inside the b-Si structure. Black silicon (b-Si) was prepared from 550 μm p-type float zone silicon wafers (100 phase, 1-5 Ω-cm) using a metal-assisted chemical etching method as described in previous literature.[22] Nano-porous b-Si with the back side protected with polyimide tape was created via the following etching steps. The Si wafer was washed with DI H_2O for 1-2 minutes before etching to get rid of impurities on the surface. The Si wafer was initially immersed into 5% HF for 90s to remove the native SiO_2, which was followed by Ag nanoparticle deposition on to the wafer in a solution containing 1 mM

$AgNO_3$ and 1 wt % HF for 30s. After rinsing briefly with distilled H_2O, the swiss cheese type porous structure was formed by soaking the substrate in a solution containing 50 wt% HF, 30 wt% H_2O_2, isopropanol and distilled H_2O with a volume ratio of 6.5 ml: 85 µl: 5 ml: 93.5ml for 8 min. Ag NP were then eliminated by exposing the wafer to 35% HNO_3 for 6 min, rinsing with H_2O and drying under N_2. After drying the black silicon wafer was cut into pieces and electrodes sizing from 0.07-0.1 cm^2 were utilized for electrode fabrication. For photoelectrode fabrication, a back-side ohmic contact was formed by removing the polyimide tape, etching with 5% HF for 30 s, and applying a commercial Ga-In eutectic alloy (sigma-aldrich). The Ga-In eutectic attached to the back of Si wafer was then collected with a copper wire covering with a silver paint. The electrical contact was isolated from the electrolyte solution with covering with a glass tube, subsequently sealing with one insulation layer, and one-layer acid resistant epoxy coating (Loctite 9462 Hysol and E-120HP). Two types of catalysts were applied on the nano-porous b-Si for comparison purpose. Platinum deposition was conducted following a literature procedure.[22] In a typical deposition experiment, the b-Si electrodes were soaked in 5 mM H_2PtCl_6 in 1 % HF solution for 30 s under an ambient light condition. The obtained photoelectrode was washed thoroughly with distilled water (3 × 10 ml) and dried under nitrogen atmosphere. For b-Si/MoS_x electrodes, MoS_x catalysts were deposited onto the photoelectrode by the photoelectrochemical method described previously.[28]

Electron microscopy characterizations and corresponded sample preparation

Surface morphology of electroactive biofilms grown on the carbon fiber anode was characterized by a Quanta 200 FEG Environmental-SEM at Imaging & Analysis Center of Princeton University. A JEOL 2800 high throughput TEM equipped with dual high solid angle 30 mm^2 windowless Si X-ray detectors was operated in TEM and STEM modes at 200 kV for characterization of semiconductor materials. For STEM analysis, a nanometer-sized probe with a total beam current of <110 pA was used for sample analysis using the inelastically scattered electrons passing through the electron transparent sample to form a high angle annular dark field (HAADF) image, which is proportional to atomic mass. Electron dispersive X-ray spectra (EDS) was operated in the same condition to acquire the Si-*K*, O-*K*, Mo-*K,* and S *K* edges with the best achievable spatial and energy resolution. To acquire quantitative measures in a single acquisition, multiple 5-second scans over 512 x 512 pixels were performed. Cliff-Lorimer thin film correction and Thermo Scientific software were used to process the EDS spectra and calculate weighted atomic percent spectral maps. Weighted spectral images were visualized using Matlab. These nominalized maps were compared against the accompanying HAADF image, and the quantitative differences of particles, tracks, and pores can be visualized.

Electron transparent TEM thin foils were prepared using a FEI Helios Dual Beam focus ion beam (FIB) instrument. Samples were coated with a layer of carbon to improve sample conductivity and minimize sample drift inside the FIB. Inside the FIB, a gradient of fine to coarse grained ion beam platinum layers were deposited over of an area 15 μm by 3 μm with a

thickness of 3 μm. A thin foil lifts out proceeded over this rectangular area with final lamellae measured as 13 μm by 5 μm. Less than 100 nm in total thickness was lifted and mounted to a molybdenum Omniprobe TEM grid for examination. A final cleaning was performed using a 5 kV gallium beam and a beam current of 12 pA to remove material deposits during FIB preparation and reduce milling damage.

The JEOL 2800 was also used to collected energy dispersive X-ray maps using an analytical probe size measuring 1.2 nm with a beam current exceeding 15 picoamperes. The X-ray maps were collected using the Thermo Scientific EDS software and the 512 × 512 pixel maps were calculated in net counts after polynomial background subtraction as demonstrated by figure 2 and figure 3. Analytical electron energy loss microscopy was performed on the aberration corrected JEOL ARM microscope, equipped with a Gatan Enfinium electron energy loss image filter (GIF), at UC Irvine. This instrument was mostly used for EELS measurement. Higher resolution Scanning TEM high angle annular dark field (HAADF) and electron energy loss (EEL) spectral imaging were performed using an analytical probe size of 0.9 Angstroms. The EELS density maps were calculated using the Gatan Digital Micrograph and rendered in Matlab. Interestingly, higher magnification STEM images looking perpendicular to a tunnel show that the amorphous SiO_x form continues nanoparticle sizing from 3-5 nm inside the wall of the “swiss cheese” tracks (Fig. S3c, d).

Inductively coupled plasma mass spectrometry: The inductively coupled plasma mass spectrometry (ICP-MS) experiment was conducted on a Perkin-Elmer Sciex/Elan 9000 DRCe with a Perkin Elmer AS93 plus autosampler. Molybdenum, platinum, and standards were prepared from Inorganic Ventures MS Mo-10 ppm and Pt-10 ppm, respectively. The samples were run in standard (STD) mode with Collision Cell Technology (CCT). The ICP-MS samples were prepared by dissolving silicon photoelectrode into aqua regia digestion solution (0.58 ml) overnight and diluting it to 30 ml for analysis. The detailed electrolysis data and TON/TOF values are summarized in Table S1. The total charge of 90 h, which further used to estimate the amount of H_2 evolution, was obtained from integrating the photocurrent over time. On the basis of catalyst loading measured by ICP-MS, the Pt and MoS_x catalysts loading amounts were 67.80 nmol/cm^2 and 97.16 nmol/cm^2, respectively. To estimate the lower bound of the Turnover number (TON) and Turnover frequency (TOF) for the HER, all loaded catalysts were assumed to contribute to the 90-h electrolysis performance and the faradaic efficiency was assumed to be 100%. The calculated average turnover number (TON) and average turnover frequency (TOF) for 90 h were 388768 and 1.20 s^{-1} for b-Si/Pt and 495471 and 1.53 s^{-1} for b-Si/MoS_x electrode, respectively.

X-ray photoelectron Spectroscopy: X-ray photoelectron spectroscopy was performed at the

Surface Science Facility at University of California Irvine using a Kratos AXIS Supra equipped with a monochromatic Al K-alpha x-ray source at 15 kV. All XPS measurements were collected using slot (300 um x 700 um spot size) collimation and hybrid lens mode without using a charge neutralizer during acquisition. Survey scans were collected with a 1.0 eV step size, 160 eV pass energy followed by high-resolution scans with a step size of 0.1 eV, 20 eV pass energy. All spectra were shifted to the binding energy of the carbon 1s (assigned to 284.8 eV) to compensate for any off-set during measurements. The resulting XPS spectra were fitted using XPSPEAK41 software to estimate the chemical state and nature of the catalysts. All fittings followed a self-consistent method similar to our previous publication.[28]

Wastewater and electrolytes

Raw brewery wastewater (BWW) with chemical oxygen demand (COD) of 40750 ± 70 mg/L was obtained from Avery Brewing Company (Boulder CO, USA). The BWW was diluted to 2026 ± 50 mg/L in COD (1:20) with 0.2 M phosphate buffer solution (PBS, 34.56 g L^{-1} $Na_2HPO_4 \cdot 7H_2O$, 9.80 g L^{-1} $NaH_2PO_4 \cdot H_2O$, 0.31 g L^{-1} NH_4Cl, 0.13 g L^{-1} KCl) and used as the analyte in the study. In some cases, artificial wastewater (AW) containing 2.5 g L^{-1} sodium acetate and 0.2 M PBS was used as the anolyte.[43] Both wastewaters have a pH of around 7.0. The catholyte used in the study was 0.2 M H_2SO_4 with pH ~0.7.

MPEC construction and operation.

524 MPEC reactors are made of polycarbonate with cylindrical chambers (3 cm in diameter).
525 Bioanodes were carbon fiber brushes (2.5 cm diameter × 2.5 cm length, 0.22 m^2 surface area,
526 18000 m^2 m^{-3} specific surface area).[44] Bioanode-1 and photocathode were separated by a bipolar
527 membrane (Fumasep FBM, FumaTech) (Fig. 1 and S16c, d) with an electrode distance of 5 cm.
528 Air cathode is made of carbon cloth (7 cm^2, 30% wet proofing, Fuel Cell Earth, Woburn, USA)
529 with a diffusion layer and a catalyst layer (9 mg cm^{-1} NORIT A SUPRA USP active carbon and
530 1 mg cm^{-1} Vulcan XC-72 carbon black powder), which is facing the bioanode-2 with a distance
531 of 1.5 cm. There is no conductive junction between the bioanodes.
532
533 The bioanodes (Fig. S16a, b) were inoculated with anaerobic sludge from Boulder
534 Wastewater Treatment Facility and enriched with BWW and AW, respectively, in an
535 electrochemical system.[14] Each chamber of MPEC was connected with a 250 mL external
536 reservoir to enable independent electrolyte recirculation at a rate of 3 mL min^{-1} to provide
537 sufficient substrate and mass transfer (Fig. S17). All electrolytes were purged with ultrahigh
538 purity argon gas to remove dissolved oxygen before being used in the experiment. Each
539 experiment cycle was 90 h, with new analyte added at 45 h to ensure substrate supply. An
540 Ag/AgCl reference electrode (0.210 V vs. Normal hydrogen electrode (NHE), RE-5B, BASi,
541 USA) was placed in each chamber for potential measurements.[45]
542
543 **Photoelectrochemical, microbiological and chemical measurements**

A 300 W Xe-arc lamp (Newport, USA) coupled with a water filter blocking infrared irradiation was used as the solar simulator in the MPEC experiment. The intensity of the light was calibrated by an optical power meter with a thermal sensor (THORLABS, USA) to ensure an incident photo density identical to 1-sun (100 mW cm^{-2}). The Xe-arc lamp spectrum under 1 Sun condition was provided in Fig. S22. A potentiostat (Biologic VMP3) was used to perform cyclic voltammetry (CV) and linear sweep voltammetry (LSV) measurements for bioanode and photocathode.[46] All photoresponse characterizations of photoelectrode were performed in a custom-fabricated three-neck round-bottom reactor with quartz windows. A coiled platinum wire (BASi-MW-1033) served as the counter electrode, and an Ag/AgCl reference electrode (RE-5B, BASi, USA) was used as reference. E(RHE) = E(Ag/AgCl) + 0.21 V + 0.059 pH V was used to convert the measured potential to RHE reference scale. The incident photon-to-current efficiencies (IPCE) of Swiss-cheese electrodes were measured in 0.2 M H_2SO_4 solution at −0.6 V vs Ag/AgCl, where the electrode reached a saturation current and contribution from dark current is minimal. For IPCE measurements, 10 nm band-pass filters (Thorlabs-FKB-VIS-10), centered at 350, 400, 450, 500, 550, 600, 650,700, 750 and 800 nm were used. Photocurrent density at each irradiation intensity (ΔJ_λ) was monitored by finding the difference in dark and photocurrent densities at a given applied voltage bias (Figure S5A). The total photon flux (I) was measured at each wavelength by a power meter (Newport, Model 1918-R), placed at a distance equivalent to that of the working electrode. The IPCE for monochromatic light was calculated using eq 1.

$$IPCE\ \% = \frac{1240 \times \Delta J_\lambda (mA/cm^2)}{\lambda(nm) \times I\left(\frac{mW}{cm^2}\right)} \qquad (1)$$

The final IPCE % value was further calibrated by dividing the transmission of the cell with 0.2 M H_2SO_4. All related calculation data are presented in Table S3. For comparison of column and swiss-cheese interfaces, LSV was run for four times. If all four LSVs can overlap with each other is an indication that the electrode is comparable stable under the operation condition. The solar to hydrogen (STH) conversion efficiency of the photocathode (η) was calculated according to the equation: $\eta = J_{mpp}V_{mpp}/P_{in}$, where J_{mpp} (mA cm^{-2}) and V_{mpp} (V) are the current density and applied potential of photocathode at the maximum power point, and P_{in} (100 mW cm^{-2}) is the power of incident illumination.[6]

The photocurrent of MPEC was also recorded by the potentiostat by applying a 0 V bias, in which the potentiostat served as an ammeter. For convenience, all currents were reported as positive values. The electrode potential (vs. Ag/AgCl reference electrode) as well as potential differences across the electrodes and bipolar membrane were recorded by a data acquisition system (model 2700, Keithley). The bacterial community in the anode biofilm, brewery wastewater and anaerobic sludge inoculum were analyzed using high-throughput 454 GS-FLX pyrosequencing of the 16S rRNA. Bioinformatics analysis was carried out according to previously described methods.[47] The H_2 produced at the photocathode was accumulated in the reservoir headspace and measured by a micro gas flow meter (MilliGascounters, Ritter, Germany) and a gas chromatograph (Model 8610C, SRI Instruments, USA) equipped with a thermal conductivity detector.[48] Wastewater organic COD was measured using a standard method

584 (HACH Company, USA). The solution pH was measured using a pH meter (Thermo, USA). The
585 calculations of Coulombic and Faradaic efficiencies, along with other measurement details can
586 be found in Supplementary Information.

587 Acknowledgements

588 We appreciate the help from Ich C. Tran and Toshihiro Aoki at the UC Irvine Materials Research
589 Institute (IMRI) for XPS and EELS measurements. The IMRI is funded in part by the National
590 Science Foundation (NSF) Major Research Instrumentation Program under grant no.
591 CHE-1338173. We also thank Dr. Nan Yao and staff at Princeton PRISM Imaging and Analysis
592 Center for SEM measurements. J.G. acknowledges the supports from SDSU startup funds, the
593 SDSU University Grants Program, and NSF award CEBT-1704992. L.L. and Z.J.R. thank the
594 support from NSF under award CEBT-1704991.
595

596 References

597 1. W.-W. Li, H.-Q. Yu and B. E. Rittmann, *Nature*, 2015, **528**, 29-31.
598 2. Z. J. Ren and A. K. Umble, *Nature*, 2016, **529**, 25-25.
599 3. P. Romero-Lankao, T. McPhearson and D. J. Davidson, *Nat. Clim. Change*, 2017, **7**, 233.
600 4. D. Kim, K. K. Sakimoto, D. Hong and P. Yang, *Angew. Chem. Int. Ed.*, 2015, **54**, 3259-3266.
601 5. F. Wen and C. Li, *Acc. Chem. Res.*, 2013, **46**, 2355-2364.
602 6. M. G. Walter, E. L. Warren, J. R. McKone, S. W. Boettcher, Q. Mi, E. A. Santori and N. S. Lewis, *Chem. Rev.*, 2010,
603 **110**, 6446-6473.
604 7. A. Kudo and Y. Miseki, *Chem. Soc. Rev.*, 2009, **38**, 253-278.
605 8. O. Khaselev and J. A. Turner, *Science*, 1998, **280**, 425-427.
606 9. C. X. Guo, J. Xie, H. Yang and C. M. Li, *Adv. Sci.*, 2015, **2**, 1500135.
607 10. C. X. Guo, Y. Dong, H. B. Yang and C. M. Li, *Adv.Energy Mater.*, 2013, **3**, 997-1003.
608 11. W. Yuan, J. Yuan, J. Xie and C. M. Li, *ACS Appl. Mater. Interfaces*, 2016, **8**, 6082-6092.
609 12. J. Oh, T. G. Deutsch, H.-C. Yuan and H. M. Branz, *Energy Environ. Sci.*, 2011, **4**, 1690-1694.
610 13. P. Peerakiatkhajohn, J.-H. Yun, S. Wang and L. Wang, *J. Photon. Energy*, 2017, **7**, 012006-012006.
611 14. L. Lu, N. B. Williams, J. Turner, P.-C. Maness, J. Gu and Z. J. Ren, *Environ. Sci. Technol.*, 2017, **51**, 13494-13501.
612 15. J. Schneider and D. W. Bahnemann, *J. Phys. Chem. Lett.*, 2013, **4**, 3479-3483.
613 16. F. Qian, G. Wang and Y. Li, *Nano Lett.*, 2010, **10**, 4686-4691.
614 17. Q.-Y. Chen, J.-S. Liu, Y. Liu and Y.-H. Wang, *J. Power Sources*, 2013, **238**, 345-349.
615 18. H. Wang, F. Qian, G. Wang, Y. Jiao, Z. He and Y. Li, *ACS nano*, 2013, **7**, 8728-8735.
616 19. G.-L. Zang, G.-P. Sheng, C. Shi, Y.-K. Wang, W.-W. Li and H.-Q. Yu, *Energy Environ. Sci.*, 2014, **7**, 3033-3039.
617 20. Y.-R. He, F.-F. Yan, H.-Q. Yu, S.-J. Yuan, Z.-H. Tong and G.-P. Sheng, *Appl. Energy*, 2014, **113**, 164-168.
618 21. D. Liang, G. Han, Y. Zhang, S. Rao, S. Lu, H. Wang and Y. Xiang, *Appl. Energy*, 2016, **168**, 544-549.
619 22. J. A. Aguiar, N. C. Anderson and N. R. Neale, *J. Mater. Chem. A*, 2016, **4**, 8123-8129.

23. E. n. Torralba-Peñalver, Y. Luo, J.-D. Compain, S. Chardon-Noblat and B. Fabre, *ACS Catal.*, 2015, **5**, 6138-6147.
24. Y. Zhao, N. C. Anderson, M. W. Ratzloff, D. W. Mulder, K. Zhu, J. A. Turner, N. R. Neale, P. W. King and H. M. Branz, *ACS Appl. Mater. Interfaces*, 2016, **8**, 14481-14487.
25. L. Lu and Z. J. Ren, *Bioresour. Technol.*, 2016, **215**, 254-264.
26. D. A. Vermaas, M. Sassenburg and W. A. Smith, *J. Mater. Chem. A*, 2015, **3**, 19556-19562.
27. H. Han, Z. Huang and W. Lee, *Nano Today*, 2014, **9**, 271-304.
28. J. Gu, J. A. Aguiar, S. Ferrere, K. X. Steirer, Y. Yan, C. Xiao, J. L. Young, M. Al-Jassim, N. R. Neale and J. A. Turner, *Nat. Energy*, 2017, **2**.
29. C.-H. Lee, J.-M. Yun, S. Lee, S. M. Jo, K. Eom, D. C. Lee, H.-I. Joh and T. F. Fuller, *Sci. Rep.*, 2017, **7**, 41190.
30. J. H. Kim, J. Y. Cheon, T. J. Shin, J. Y. Park and S. H. Joo, *Carbon*, 2016, **101**, 449-457.
31. Y. Yang, M. Wang, P. Zhang, W. Wang, H. Han and L. Sun, *ACS Appl. Mater. Interfaces*, 2016, **8**, 30143-30151.
32. R. Fan, J. Mao, Z. Yin, J. Jie, W. Dong, L. Fang, F. Zheng and M. Shen, *ACS Appl. Mater. Interfaces*, 2017, **9**, 6123-6129.
33. L. Lu, D. Xing, N. Ren and B. E. Logan, *Bioresour. Technol.*, 2012, **124**, 68-76.
34. H. Vrubel, D. Merki and X. Hu, *Energy Environ. Sci.*, 2012, **5**, 6136-6144.
35. H.-S. Lee, W. F. J. Vermaas and B. E. Rittmann, *Trends Biotechnol.*, 2010, **28**, 262-271.
36. S. Hu, N. S. Lewis, J. W. Ager, J. Yang, J. R. McKone and N. C. Strandwitz, *J. Phys. Chem. C*, 2015, **119**, 24201-24228.
37. J. L. Young, M. A. Steiner, H. Döscher, R. M. France, J. A. Turner and T. G. Deutsch, *Nat. Energy*, 2017, **2**, 17028.
38. J. Jia, L. C. Seitz, J. D. Benck, Y. Huo, Y. Chen, J. W. D. Ng, T. Bilir, J. S. Harris and T. F. Jaramillo, *Nat. commun.*, 2016, **7**, 13237.
39. B. A. Pinaud, J. D. Benck, L. C. Seitz, A. J. Forman, Z. Chen, T. G. Deutsch, B. D. James, K. N. Baum, G. N. Baum and S. Ardo, *Energy Environ. Sci.*, 2013, **6**, 1983-2002.
40. E. L. Miller, 2017.
41. A. Moloney, F. James and J. Stelger, *Water & Wastes Digest*, September 2014.
42. U. S. DOE, *Current U.S. Hydrogen Production, DOE Hydrogen and Fuel Cells Program Record*, U.S. Department of Energy, 2012.
43. C. Forrestal, Z. Stoll, P. Xu and Z. J. Ren, *Environ. Sci.: Water Res. Technol.*, 2015.
44. L. Lu, Z. Huang, G. H. Rau and Z. J. Ren, *Environ. Sci. Technol.*, 2015, **49**, 8193-8201.
45. G. Lu, Y. Zhu, L. Lu, K. Xu, H. Wang, Y. Jin, Z. J. Ren, Z. Liu and W. Zhang, *J. Power Sources*, 2016, **315**, 302-307.
46. L. Lu, D. Hou, Y. Fang, Y. Huang and Z. J. Ren, *Electrochim. Acta*, 2016, **206**, 381-387.
47. L. Lu, T. Huggins, S. Jin, Y. Zuo and Z. J. Ren, *Environ. Sci. Technol.*, 2014, **48**, 4021-4029.
48. L. Lu, D. Hou, X. Wang, D. Jassby and Z. J. Ren, *Environ. Sci. Technol. Lett.*, 2016, **3**, 286-290.